

Chemical Vapor Deposition

Molecular Engineering of Mn^{II} Diamine Diketonate Precursors for the Vapor Deposition of Manganese Oxide Nanostructures

Chiara Maccato,^[a] Lorenzo Bigiani,^[a] Giorgio Carraro,^[a] Alberto Gasparotto,^[a] Roberta Seraglia,^[b] Jiyeon Kim,^[c] Anjana Devi,^[c] Gloria Tabacchi,^{*,[d]} Ettore Fois,^[d] Giuseppe Pace,^[b] Vito Di Noto,^[e] and Davide Barreca^{*,[b]}

Abstract: Molecular engineering of manganese(II) diamine diketonate precursors is a key issue for their use in the vapor deposition of manganese oxide materials. Herein, two closely related β -diketonate diamine Mn^{II} adducts with different fluorine contents in the diketonate ligands are examined. The target compounds were synthesized by a simple procedure and, for the first time, thoroughly characterized by a joint experimental–theoretical approach, to understand the influence of the ligand on their structures, electronic properties, thermal behavior, and reactivity. The target compounds are monomeric and exhibit a pseudo-octahedral co-

ordination of the Mn^{II} centers, with differences in their structure and fragmentation processes related to the ligand nature. Both complexes can be readily vaporized without premature side decompositions, a favorable feature for their use as precursors for chemical vapor deposition (CVD) or atomic layer deposition applications. Preliminary CVD experiments at moderate growth temperatures enabled the fabrication of high-purity, single-phase Mn₃O₄ nanosystems with tailored morphology, which hold great promise for various technological applications.

Introduction

Manganese oxide nanomaterials are of considerable importance for many technological applications thanks to their diversified structures and variety of appealing chemical and physical properties.^[1] In particular, Mn₃O₄, a mixed-valence oxide with a tetragonal structure, has received attention thanks to its durability, low cost, and attractive performances for a variety of end uses, spanning from (photo)catalysts,^[1a,b,2]

to anodes of lithium-ion batteries and pseudocapacitors,^[1b,2b,3] up to electrochromic systems,^[4] magnetic media,^[5] and gas sensors.^[1d,6] In this widespread context, the fabrication of Mn₃O₄ nanostructures with tailored morphology (nanoparticles, nanorods, nanofractals, etc.) has been performed by a variety of synthetic techniques, encompassing microwave irradiation, hydrothermal/solvothermal routes, chemical bath deposition, and chemical vapor deposition (CVD).^[1a,b,2a,c,4–7] In particular, the latter process, along with atomic layer deposition (ALD), is compatible with current processing standards, thanks to the capability of achieving in situ, large-area growth of thin films and nanostructured materials with controlled properties.^[8] In this regard, the development of suitable precursor compounds endowed with high volatility, thermal stability, and clean decomposition pathways is a very challenging research area,^[9] which would ideally guide, in a “molecular engineering” approach, the modulation of material properties in view of the desired functional applications.

To date, the most used CVD and ALD Mn precursors are mainly based on β -diketonate derivatives,^[1e,10] some of which suffer from poor shelf-life and/or unfavorable thermal properties,^[9e] especially if they contain Mn^{II}. In fact, Mn^{II} complexes with nonfluorinated β -diketonate ligands are reported to readily decompose into Mn^{III} derivatives,^[10d,11] yielding poor control of the phase composition of the product. As a consequence, the obtainment of single-phase Mn₃O₄ nanomaterials with controlled crystallinity and morphology^[12] requires the tailoring of β -diketonate compound properties at the molecular level. In this regard, the use of fluorinated ligands, such as 1,1,1,5,5,5-hexafluoro-2,4-pentanedionate (hfa), is favorable for the ob-

[a] Prof. C. Maccato, Dr. L. Bigiani, Dr. G. Carraro, Prof. A. Gasparotto
Department of Chemical Sciences, Padova University and INSTM
35131 Padova (Italy)

[b] Dr. R. Seraglia, Dr. G. Pace, Dr. D. Barreca
CNR-ICMATE and INSTM, Department of Chemical Sciences,
Padova University, 35131 Padova (Italy)
E-mail: davide.barreca@unipd.it

[c] Dr. J. Kim, Prof. A. Devi
Inorganic Materials Chemistry
Faculty of Chemistry and Biochemistry
Ruhr-University Bochum, 44801 Bochum (Germany)

[d] Prof. G. Tabacchi, Prof. E. Fois
Department of Science and High Technology
University of Insubria and INSTM
22100 Como (Italy)
E-mail: gloria.tabacchi@uninsubria.it

[e] Prof. V. Di Noto
Department of Industrial Engineering
Chemical Technology Section
Department of Chemical Sciences, Padova University and INSTM
35131 Padova (Italy)

Supporting information and the ORCID identification number(s) for the author(s) of this article can be found under:
<https://doi.org/10.1002/chem.201703423>

tainment of metal complexes with improved shelf-life, thermal and mass-transport properties relative to those of nonfluorinated compounds.^[9e] The hfa ligand has two $-\text{CF}_3$ groups, which enhance volatility through a decrease in van der Waals intermolecular forces^[10d] and result in enhanced Lewis acidity of the metal center,^[9e] enabling the effective binding of diamine Lewis bases, such as *N,N,N',N'*-tetramethylethylenediamine (TMEDA). The introduction of the latter enables a complete saturation of the metal coordination sphere, yielding β -diketonate-diamine compounds with the general formula $\text{M}(\text{hfa})_2\cdot\text{TMEDA}$, which feature higher stability towards hydrolysis and provide improved thermal/mass-transport properties,^[13] important characteristics for their use as CVD precursors.

In our previous studies, we devoted our attention to $\text{M}(\text{hfa})_2\cdot\text{TMEDA}$ complexes of various elements, in particular, Cu ,^[13a,14] Co ,^[13b] Fe ,^[15] and Zn .^[16] Although all of these molecular systems present a common structural motif, that is, a pseudo-octahedral MO_4N_2 geometry, investigations have provided evidence that specific physicochemical properties, as well as the features of the obtained CVD products, significantly depend on the nature of the metal center. Even in the case of manganese, stable Mn^{II} compounds can be obtained by using fluorinated diketonate ligands, such as hfa.^[9e,11,17] Now, the question arises as to whether the presence of only one $-\text{CF}_3$ group for each diketonate could be sufficient to endow the diamine adducts with the stability, volatility, and clean decomposition properties required for CVD/ALD applications. If the weakest bonds of the complex, that is, the first to be broken, depend on the metal center,^[14b,15c,16] the effect of the ligand is equally important. Notably, a diketonate with a single $-\text{CF}_3$ group (indicated hereafter as tfa = 1,1,1-trifluoro-2,4-pentanedionate) could be formally obtained by replacing one of the hfa fluorinated moieties with a methyl group. How would such a ligand modify the chemistry of these precursors, and to what extent would their CVD performances be affected? Literature, unfortunately, offers no clear answer to these questions. Though $\text{M}(\text{tfa})_2$ complexes have been reported for $\text{M} = \text{Co}$,^[18] Ni ,^[19] and Cu ,^[20] $\text{M}(\text{tfa})_2\cdot\text{TMEDA}$ adducts have been much less studied than their hfa-containing counterparts. In fact, only one study of $\text{Cu}(\text{tfa})_2\cdot\text{TMEDA}$ has been reported so far,^[21] and no direct connections between ligand properties and precursor behavior have been investigated in detail.

To elucidate such inter-relations, we investigate herein the structure/property interplay for two Mn^{II} complexes with either hexa- or trifluorinated diketonate ligands, namely, $\text{Mn}(\text{hfa})_2\cdot\text{TMEDA}$ and $\text{Mn}(\text{tfa})_2\cdot\text{TMEDA}$. It is worthwhile noting that, despite the preparation of $\text{Mn}(\text{hfa})_2\cdot\text{TMEDA}$ has already been reported,^[22] only some data on its structure and thermal behavior are available in the literature,^[11,17] whereas a detailed theoretical-experimental characterization of this compound is completely missing. The need for these studies is even more relevant for $\text{Mn}(\text{tfa})_2\cdot\text{TMEDA}$, which, so far, has been mentioned only once in a patent as an antiknock additive.^[22]

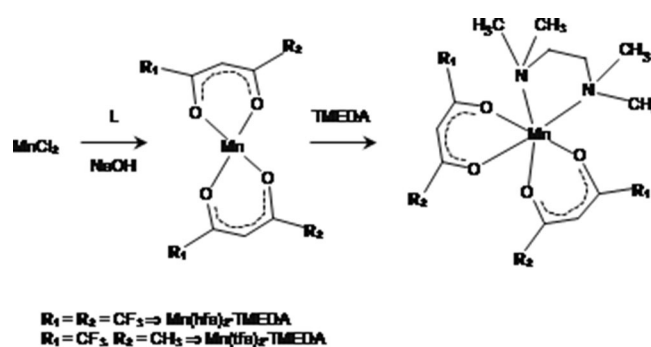
Herein, our main aim is to disclose how the degree of fluorination of the ligand in $\text{MnL}_2\cdot\text{TMEDA}$ precursors affects their physicochemical features, including stability, volatility, and gas-phase fragmentation, with particular attention to their per-

formances in the CVD of Mn_3O_4 nanomaterials. Experimental results presented herein for the two complexes are validated and integrated with detailed density functional theory (DFT) modeling, with the aim of providing a theoretical basis^[23] for the interpretation of similarities and differences in their structure, bonding, and chemical behavior. Finally, preliminary data concerning the low-pressure CVD validation of both compounds as Mn molecular sources for high-purity Mn_3O_4 nano-deposits on different substrates are also reported.

Results and Discussion

Synthesis and characterization of $\text{MnL}_2\cdot\text{TMEDA}$ compounds

Herein, $\text{MnL}_2\cdot\text{TMEDA}$ adducts were synthesized through a procedure different from that reported in the literature for $\text{Mn}(\text{hfa})_2\cdot\text{TMEDA}$,^[17] involving the reaction in aqueous mixtures between Mn^{II} chloride and L ligands in the presence of TMEDA (Scheme 1). The process, which was carried out at room tem-



Scheme 1. The synthesis of $\text{MnL}_2\cdot\text{TMEDA}$ derivatives.

perature with no need for heating at reflux, at variance with a previous study,^[11] yielded the target adducts, which could be readily manipulated in the presence of air, moisture, and light without any detrimental degradation. Apart from a shelf-life of several months, an important feature for CVD applications, the present $\text{MnL}_2\cdot\text{TMEDA}$ compounds possessed an appreciable volatility (m.p. = 86 and 99 °C for L = hfa and tfa, respectively^[22]) and could be readily sublimed under vacuum ($\approx 10^{-3}$ mbar). The melting point of $\text{Mn}(\text{hfa})_2\cdot\text{TMEDA}$ at atmospheric pressure was higher than that previously obtained by some investigators,^[11,17] but in line with that reported in a patent quoting the use of this compound as a gasoline additive.^[22]

The molecular structures of the two complexes are displayed in Figure 1, whereas crystallographic and structural refinement data, as well as geometrical parameters of DFT-calculated structures, are presented in Tables S1 and S2 in the Supporting Information. Selected bond lengths and angles are listed in Table 1. At variance with other cases, such as that of Mn bis(*N,N'*-diisopropylacetamidate)^[24] or variously substituted dialkylmanganese(II) complexes,^[8d] both compounds were monomeric both in the solid state and in solution [see below for electrospray ionization-mass spectrometry (ESI-MS) results], which indicated that the use of TMEDA was effective in satu-

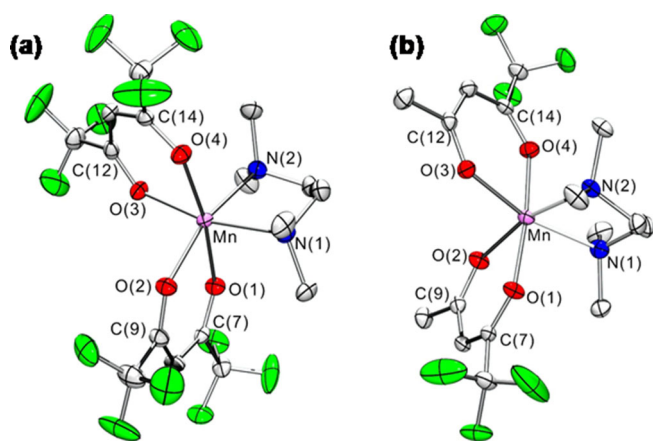


Figure 1. Molecular structures of a) $\text{Mn}(\text{hfa})_2 \cdot \text{TMEDA}$ and b) $\text{Mn}(\text{tfa})_2 \cdot \text{TMEDA}$. Displacement ellipsoids are shown at the 50% probability level. Hydrogen atoms and rotational disorder from $-\text{CF}_3$ groups are omitted for clarity.

Table 1. Selected bond lengths and angles for $\text{Mn}(\text{hfa})_2 \cdot \text{TMEDA}$ and $\text{Mn}(\text{tfa})_2 \cdot \text{TMEDA}$.		
	$\text{Mn}(\text{hfa})_2 \cdot \text{TMEDA}$	$\text{Mn}(\text{tfa})_2 \cdot \text{TMEDA}$
bond lengths [Å]		
Mn–O(1)	2.1472(14)	2.1481(14)
Mn–O(2)	2.1743(14)	2.1629(14)
Mn–O(3)	2.1546(14)	2.1525(14)
Mn–O(4)	2.1493(14)	2.1265(14)
Mn–N(1)	2.2984(17)	2.3428(18)
Mn–N(2)	2.2989(17)	2.3116(17)
O(1)–C(7)	1.251(2)	1.261(2)
O(2)–C(9)	1.245(2)	1.255(2)
O(3)–C(12)	1.244(3)	1.252(2)
O(4)–C(14)	1.248(3)	1.260(2)
bond angles [°]		
O(1)–Mn–O(2)	82.07(5)	83.21(6)
O(3)–Mn–O(4)	82.60(5)	83.52(6)
N(1)–Mn–N(2)	79.81(6)	78.66(6)
O(1)–Mn–O(4)	171.03(5)	173.85(6)
O(3)–Mn–N(1)	167.48(5)	166.57(6)
O(2)–Mn–N(2)	166.34(6)	166.49(6)
Mn–O(1)–C(7)	130.02(13)	127.70(13)
Mn–O(2)–C(9)	129.06(13)	130.70(13)
Mn–O(3)–C(12)	128.78(13)	131.12(13)
Mn–O(4)–C(14)	129.13(13)	127.72(13)

rating the Mn^{II} coordination sphere. In addition, though the synthesis was carried out in aqueous mixtures, no water molecules were present in the Mn^{II} environment and no classical hydrogen bonds formed in the solid-state structure. The latter feature is of key importance in view of CVD/ALD utilization^[13,15a] (see below for thermoanalytical data). In contrast, for $\text{Mn}(\text{hfa})_2 \cdot 2\text{H}_2\text{O}^{[10d]}$ and other Mn^{II} β -diketonates, such as adducts of $\text{Mn}(\text{hfa})_2$ with substituted nitronyl nitroxides,^[25] the occurrence of hydrogen bonding has been observed.

For both structures shown in Figure 1, X-ray crystal-structure determination provided evidence of a *cis* geometry,^[26] as also reported for $\text{M}(\text{hfa})_2 \cdot \text{TMEDA}$ with $\text{M} = \text{Fe},^{[15a]}$ $\text{Co},^{[13b]}$ and $\text{Cu},^{[13a]}$ with a twofold axis bisecting the TMEDA ligand. Irrespective of

the β -diketonate used, the mean Mn–O and Mn–N bond lengths were in agreement with those obtained for coordination complexes of 2-(4-quinolyl)nitronyl nitroxide^[27] and 2,2'-bipyridine^[28] with $\text{Mn}(\text{hfa})_2$ and for various $\text{Mn}^{\text{II}}\text{-hfa}$ compounds, including $\text{Mn}(\text{hfa})_2 \cdot \text{TMEDA},^{[9e,10d,17,26]}$ although this study contains a better quality of structure refinement for the latter complex. As observed in Figure 1, both compounds presented a sixfold coordination around the Mn^{II} centers, resulting in a MnO_4N_2 distorted octahedral environment, in line with previous reports for homologous complexes available in the Cambridge Structural Database.^[26] In comparison to other $\text{ML}_2 \cdot \text{TMEDA}$ adducts ($\text{M} = \text{Fe},^{[15a]}$ $\text{Co},^{[13b]}$ $\text{Cu},^{[13a]}$ $\text{Zn}^{[29]}$), the O–M–O, O–M–N, and N–M–N bond angles (Table 1) are slightly lower (up to $\approx 5^\circ$), whereas M–O and M–N distances are longer. Similarly to the Fe homologue,^[15a] the O–C bond lengths of β -diketonate ligands were all close to 1.25 Å, a value that suggests a double-bond character (typical O–C single bonds ≈ 1.40 Å). For both compounds, the atomic distances between O(1)–C(7) and O(4)–C(14) are slightly longer than those of O(2)–C(9) and O(3)–C(12), due to $-\text{CF}_3$ electron-withdrawing groups being directly bonded to C(7) and C(14) atoms. In addition, Mn–O(2) and Mn–O(3) distances were slightly longer than those *trans* to the O atoms of L ligands [Mn–O(1) and Mn–O(4), Table 1^[9e]]. A similar *trans* effect has already been observed for $\text{M}(\text{hfa})_2 \cdot \text{TMEDA}$ compounds with $\text{M} = \text{Mg},^{[30]}$ $\text{Fe},^{[15a]}$ $\text{Co},^{[13b]}$ and $\text{Zn}.^{[16,29]}$ Finally, it is worth noting that, for both complexes, Mn–N bonds were longer than those of Mn–O. This effect, which was particularly evident for $\text{Mn}(\text{tfa})_2 \cdot \text{TMEDA}$, anticipated an easier opening of the TMEDA ring with respect to that of the β -diketonate one, as suggested by the calculated bond orders, electronic population analyses, and decomposition energies for the two precursors. In both complexes, especially for $\text{Mn}(\text{tfa})_2 \cdot \text{TMEDA}$, the diketonate is a stronger electron donor towards Mn, compared with that of the diamine (Table S3 in the Supporting Information). Accordingly, Mn–N bonds are significantly weaker than those of Mn–O (Table S4 in the Supporting Information), which suggests that, at least in the gas phase, the TMEDA ligand should be more easily released than the diketonate one. On this basis, we calculated the precursor decomposition energy (ΔE) for the pathways shown in Equations (1) and (2), with $\text{L} = \text{hfa}/\text{tfa}$, in vacuum and in methanol, that is, the solvent used in the present ESI-MS experiments:



The geometries of $\text{MnL} \cdot \text{TMEDA}^+$ and MnL_2 fragments were initially optimized in vacuum. The loss of one ligand strongly desaturates the manganese coordination sphere, and all fragments exhibit a tetrahedral coordination, as depicted in Figure S1 in the Supporting Information. For $\text{L} = \text{hfa}$, calculations yielded $\Delta E_1 = 125.4 \text{ kcal mol}^{-1}$ and $\Delta E_2 = 38.0 \text{ kcal mol}^{-1}$, whereas the corresponding values for $\text{L} = \text{tfa}$ were $\Delta E_1 = 131.3 \text{ kcal mol}^{-1}$ and $\Delta E_2 = 31.0 \text{ kcal mol}^{-1}$. Hence, in the gas phase, the loss of a hfa/tfa moiety would be significantly disfavored with respect to the loss of TMEDA, in line with previously discussed

data. Nevertheless, when the same quantities are calculated in methanol,^[31] the difference substantially decreases, which indicates that the energies involved in the two decomposition routes become comparable. This is particularly evident for L = hfa, for which $\Delta E_1 = 30.3 \text{ kcal mol}^{-1}$ and $\Delta E_2 = 28.8 \text{ kcal mol}^{-1}$, whereas for L = tfa we found values of $\Delta E_1 = 32.9 \text{ kcal mol}^{-1}$ and $\Delta E_2 = 23.3 \text{ kcal mol}^{-1}$. The reaction medium therefore has a key influence on the fragmentation pathways. The fragmentation route in Equation (1), highly disfavored in vacuum, becomes viable in a polar solvent due to stabilization of the resulting ionic species. This might be particularly important for ESI-MS experiments, in which the first fragmentation of the complex occurs in the solvent (see below). On the other hand, the route in Equation (2) should be favored in the gas phase, such as in thermal CVD experiments.

UV/Vis optical spectra of the compounds are displayed in Figure 2. The broad band at $\lambda \approx 300 \text{ nm}$, due to electronic states mostly localized on the diketonate ligands (Figure 2b, inset), arises from $\pi-\pi^*$ ligand-to-ligand excitations (see Figures S2–S4 in the Supporting Information). The calculated spectra reproduce the experimental trend, with a spectral shift to higher wavelengths for $\text{Mn(hfa)}_2\cdot\text{TMEDA}$ compared to $\text{Mn(tfa)}_2\cdot\text{TMEDA}$, and the agreement is further improved by taking into account the solvent contribution. The same trend is found for the $\pi-\pi^*$ transitions in isolated hfa and tfa (see Figure S4 in the Supporting Information), which indicates that the compound electronic excitation and optical properties are significantly influenced by the ligand nature.

This finding prompted us to investigate more closely the ligand effect on the electronic structures and electric dipole

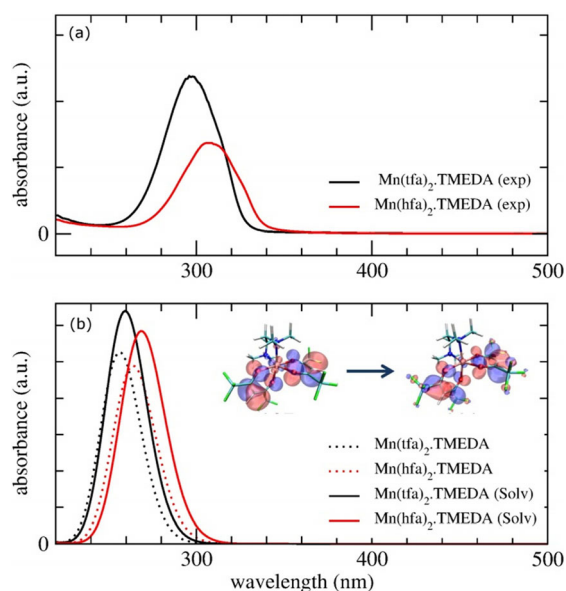


Figure 2. Experimental (a) and theoretical (b) UV/Vis optical spectra for $\text{Mn(hfa)}_2\cdot\text{TMEDA}$ (red lines) and $\text{Mn(tfa)}_2\cdot\text{TMEDA}$ (black lines). The orbitals involved in one of the components of the transition state for $\text{Mn(hfa)}_2\cdot\text{TMEDA}$ are shown in the inset of b) (see Figures S2 and S3 in the Supporting Information for graphical representations of all components for the two complexes). Theoretical spectra were calculated both in vacuum (no label) and with a polarizable continuum model^[31] for the solvent ethanol (label 'Solv').

moments of the complexes. The results showed that $\text{Mn(hfa)}_2\cdot\text{TMEDA}$ had a dipole moment considerably larger than that of $\text{Mn(tfa)}_2\cdot\text{TMEDA}$, due to the net charge separation between hfa and diamine ligands, as depicted in the electrostatic potential maps (Figure 3). Indeed, whereas the electro-

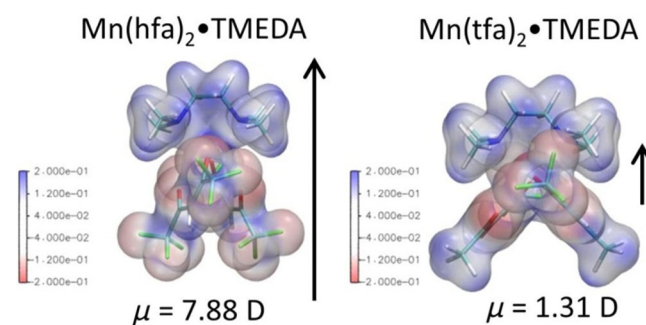


Figure 3. Electrostatic potential maps for $\text{Mn(hfa)}_2\cdot\text{TMEDA}$ and $\text{Mn(tfa)}_2\cdot\text{TMEDA}$. Regions of high (positive) potential (in blue) are electron poor, whereas regions of low (negative) potential (in red) are electron rich. White/gray colors represent intermediate electrostatic potential values. Arrows mark the direction and magnitude of electric dipole moments, μ . Atom color codes: Mn = pink; F = green; O = red; N = blue; C = cyan; H = white.

static potentials of TMEDA and hfa are positive and negative, respectively, the tfa ligand exhibits both positive and negative regions, which are localized on the $-\text{CH}_3$ and $-\text{CF}_3$ groups, respectively. Hence, the application of external electric fields, as in ESI-MS experiments (see below), might have different effects on the two compounds. Calculations indicated that both complexes were slightly stabilized by a moderate electric field, and showed a slight dipole moment increase, especially in the case of $\text{Mn(hfa)}_2\cdot\text{TMEDA}$ (see Table S5 in the Supporting Information). Such an electric field would therefore favor a preferential orientation of the complexes, with an enhanced effect for $\text{Mn(hfa)}_2\cdot\text{TMEDA}$ due to its more asymmetric charge distribution (Figure 3).

An additional insight into the behavior of the two manganese complexes was obtained by means of ESI-MS, a soft ionization technique that provided important clues about the compound reactivity. ESI-MS analyses were carried out in both positive (+) and (−) ion modes, with the aim of elucidating the adduct fragmentation pathways and their interplay with molecular structures. It is worthwhile observing that, to the best of our knowledge, no such investigation on $\text{MnL}_2\cdot\text{TMEDA}$ compounds has ever been reported in the literature to date.

In positive-ion mode, the behavior of the two compounds was qualitatively similar, irrespective of the ligand nature. The ESI(+) mass spectra (Figure 4) are dominated by single signals centered at m/z 378 and 324, which correspond to $[\text{Mn(hfa)}\cdot\text{TMEDA}]^+$ and $[\text{Mn(tfa)}\cdot\text{TMEDA}]^+$, respectively. This result agreed with those previously obtained for analogous $\text{M(hfa)}_2\cdot\text{TMEDA}$ compounds, with $\text{M} = \text{Cu}$ and Co .^[13,14]

To gain a deeper insight into the complex fragmentation pathways, MS^2 and MS^3 experiments were carried out on $[\text{MnL}\cdot\text{TMEDA}]^+$ ions (see Figures S5 and S6 in the Supporting

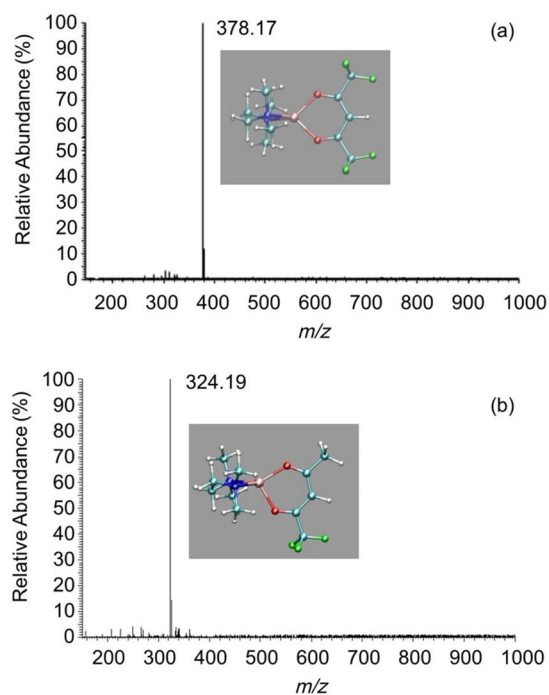


Figure 4. Positive-ion ESI-MS spectra of solutions of a) $\text{Mn}(\text{hfa})_2\text{-TMEDA}$ and b) $\text{Mn}(\text{tfa})_2\text{-TMEDA}$ in methanol. Calculated optimized structures for the most abundant ionic species are shown in the insets. Atom color codes are the same as those used in Figure 3.

Information). Irrespective of the ligand nature, MS^2 spectra were characterized by the presence of ions at m/z 190 and 115, corresponding to diamine-related derivatives, with the first one arising from a ligand-to-metal fluorine transfer process. This behavior was directly dependent on the metal nature, since similar MS^2 experiments on $[\text{M}(\text{hfa})\cdot\text{TMEDA}]^+$ ions yielded $[\text{CuTMEDA-H}]^+$, for the Cu derivative,^[13a,14a] and $[\text{CoF}_2\cdot\text{TMEDA} + \text{H}]^+$, for the Co one.^[13b]

In negative-ion mode, $\text{MnL}_2\text{-TMEDA}$ ESI-MS spectra revealed a different influence of hfa/tfa ligands on the fragmentation pathway. The ESI(-) mass spectrum of $\text{Mn}(\text{hfa})_2\text{-TMEDA}$ (Figure 5a) was characterized by the presence of ions at m/z 676 and 207, corresponding to $[\text{Mn}(\text{hfa})_3]^-$ and $[\text{hfa}]^-$, respectively. Conversely, the corresponding spectrum of $\text{Mn}(\text{tfa})_2\text{-TMEDA}$ (Figure 5b) displayed only the signal at m/z 153, corresponding to $[\text{tfa}]^-$ ions. MS/MS analyses on $[\text{Mn}(\text{hfa})_3]^-$ ions yielded the sole hfa⁻ (see Figure S7 in the Supporting Information), in line with previous results obtained in the ESI-MS analysis of $\text{Fe}(\text{hfa})_2\text{-TMEDA}$.^[15a] Different behavior of the two complexes emerging from the results shown in Figure 5 suggested a different binding capacity of hfa and tfa ligands towards Mn^{II} center. Indeed, both $[\text{MnL}_3]^-$ adducts were predicted to be stable with respect to the separated L⁻ and MnL_2 fragments, but the calculated formation energies differed by 2.0 kcal mol⁻¹ in methanol (7.4 kcal mol⁻¹ in vacuum) in favor of $[\text{Mn}(\text{hfa})_3]^-$ (see Figure S8 in the Supporting Information). Furthermore, since the formation of $[\text{MnL}_3]^-$ adducts would involve the fragmentation of at least two $\text{MnL}_2\text{-TMEDA}$ molecules, it might be argued that the higher $\text{Mn}(\text{hfa})_2\text{-TMEDA}$ dipole moment could promote a head-to-tail alignment of two such molecules, en-

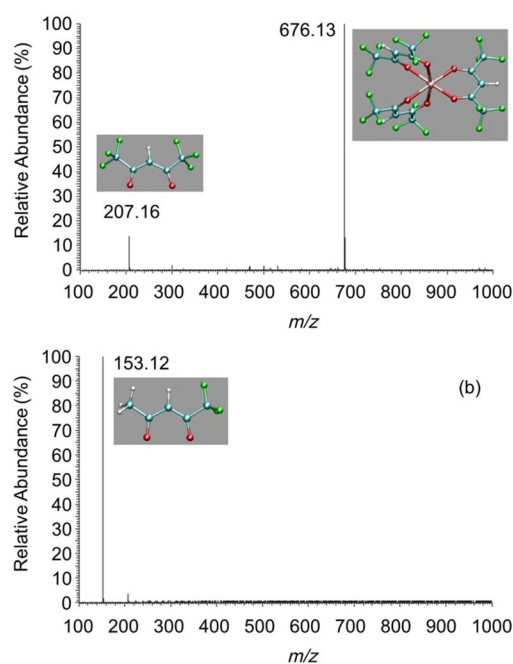


Figure 5. Negative-ion ESI-MS spectra of solutions of a) $\text{Mn}(\text{hfa})_2\text{-TMEDA}$ and b) $\text{Mn}(\text{tfa})_2\text{-TMEDA}$ in methanol. Calculated optimized structures for the most abundant ionic species are shown in the insets. Atom color codes are the same as those used in Figure 3.

hancing the probability of a successful TMEDA/hfa ligand exchange leading to the observed anion. Finally, it is worth noting that no dimer/polynuclear species have ever been detected. Considering the ESI-MS soft ionization conditions, this result suggests that both complexes are monomeric, in agreement with structural analyses (see above).

To be successfully employed as CVD/ALD precursors, the target compounds should possess sufficient stability to ensure vaporization free from undesired side decomposition, as well as a constant and reproducible vapor supply. To investigate the precursor thermal properties as a function of the ligand nature, thermogravimetric analysis (TGA) was performed on both $\text{MnL}_2\text{-TMEDA}$ compounds, yielding very similar results for freshly synthesized and aged sample batches. As observed in Figure 6a, both target adducts displayed an analogous behavior, characterized by a single-step mass loss for $T \geq 120^\circ\text{C}$, indicating a high volatility. For $\text{Mn}(\text{hfa})_2\text{-TMEDA}$, the residual weight was close to zero for $T \geq 150^\circ\text{C}$, evidencing the occurrence of clean and quantitative vaporization in a narrow temperature range. The latter phenomenon is a key advantage in view of CVD/ALD applications, especially in comparison with commonly used Mn precursors, which show either lower volatility [as observed for $\text{Mn}(\text{dpm})_3$; dpm = 2,2,6,6-tetramethyl-3,5-heptanedionate] or multi-stage decompositions, with a high residual weight [as observed for $\text{Mn}(\text{acac})_2(\text{H}_2\text{O})_2$; acac = 2,4-pentanedionate].^[10c,11] Differential scanning calorimetry (DSC) analyses (not reported) enabled us to identify the presence of two endothermic peaks at 84.5 and 100.6 °C for $\text{Mn}(\text{hfa})_2\text{-TMEDA}$ and $\text{Mn}(\text{tfa})_2\text{-TMEDA}$, respectively, related to melting processes. In line with melting point values, $\text{Mn}(\text{tfa})_2\text{-TMEDA}$ presented a slightly higher volatilization onset

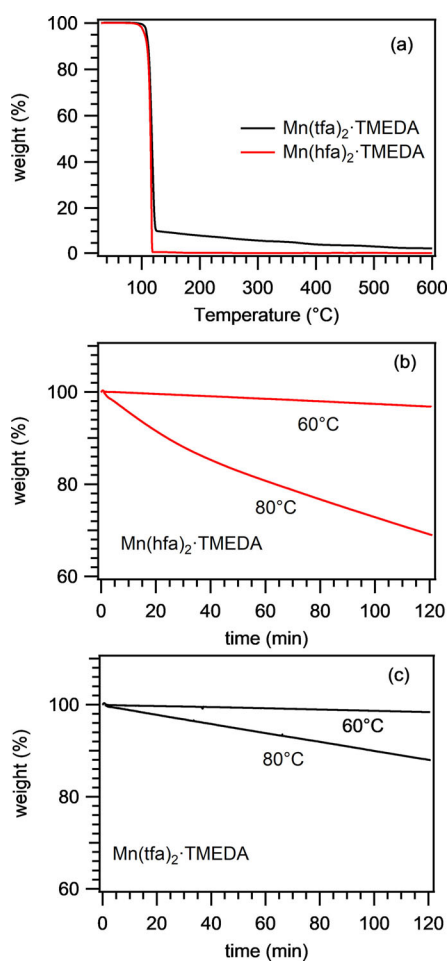


Figure 6. a) TGA profiles for $\text{MnL}_2\text{-TMEDA}$ complexes. Isothermal weight changes recorded for b) $\text{Mn(hfa)}_2\text{-TMEDA}$ and c) $\text{Mn(tfa)}_2\text{-TMEDA}$.

than $\text{Mn(hfa)}_2\text{-TMEDA}$, in line with the lower fluorine content of the former compound (see above).^[10d] In addition, a non-zero residual weight, progressively lowering from 130 to 600 °C, could be observed.

Isothermal analyses (Figure 6b and c) carried out for 2 h evidenced a nearly constant weight loss as a function of time for both compounds. Such results, in line with previous reports on Fe, Co, and Cu hfa derivatives,^[13,15a] enabled us to rule out detrimental decomposition phenomena and confirmed the occurrence of clean vaporization, an important feature for CVD/ALD applications.

CVD depositions from $\text{MnL}_2\text{-TMEDA}$

An important point of this study is the functional validation of $\text{MnL}_2\text{-TMEDA}$ compounds to assess their potential as CVD precursors for the fabrication of manganese oxide nanosystems. Preliminary deposition experiments were carried out on both Si(100) and SiO_2 substrates, by using vaporization ($\leq 65^\circ\text{C}$) and growth (400°C) temperatures lower than those previously adopted in vapor phase processes from conventional manganese precursors, such as Mn(hfa)_2 and Mn(dpm)_3 , and also from $\text{Mn(hfa)}_2\text{-TMEDA}$.^[1e,10a,b,e,11,17] The obtained brownish sam-

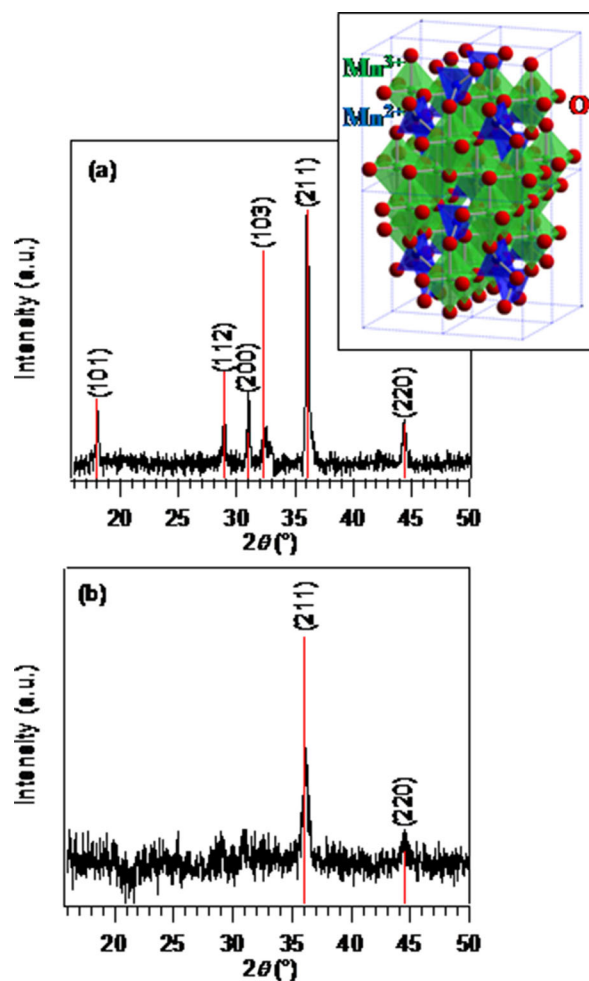


Figure 7. Glancing-angle XRD patterns of Mn_3O_4 systems deposited at 400°C : a) on Si(100), from $\text{Mn(hfa)}_2\text{-TMEDA}$; and b) on SiO_2 , from $\text{Mn(tfa)}_2\text{-TMEDA}$. Vertical bars mark the relative intensities of the Mn_3O_4 powder spectrum. Inset: representation of the Mn_3O_4 solid-state structure.^[B2]

ples, characterized by a good adhesion to the substrate, were preliminarily investigated by X-ray diffraction (XRD, Figure 7), which revealed the formation of body-centered tetragonal Mn_3O_4 [hausmannite; space group: $I4_1/amd$; ^[1a,2a,32] lattice parameters $a = 5.762 \text{ \AA}$, $c = 9.470 \text{ \AA}$; average crystallite size = $(40 \pm 5) \text{ nm}$], with Mn^{III} and Mn^{II} centers in octahedral and tetrahedral sites, respectively^[2b,5b,7] (Figure 7, inset). Irrespective of the substrate used, no reflections related to other Mn oxides or Mn^{II} fluoride could be detected, indicating the obtention of phase-pure systems, as also confirmed by X-ray photoelectron spectroscopy (XPS; see Figure S9 in the Supporting Information). The system morphology, analyzed by means of field emission-scanning electron microscopy (FE-SEM, Figure 8a and b), revealed the presence of well interconnected lamellar structures [average dimensions = $(270 \pm 50) \text{ nm}$] uniformly distributed over the substrate surface. From the mean nanodeposit thickness [$(350 \pm 20) \text{ nm}$], an average growth rate of 6 nm min^{-1} could be estimated.

The compositional purity of Mn_3O_4 systems was confirmed by EDXS analysis. The obtained spectrum (Figure 8c) showed the presence of $\text{Mn}_{\text{K}\alpha}$ and $\text{Mn}_{\text{K}\beta}$ peaks located at 5.90 and

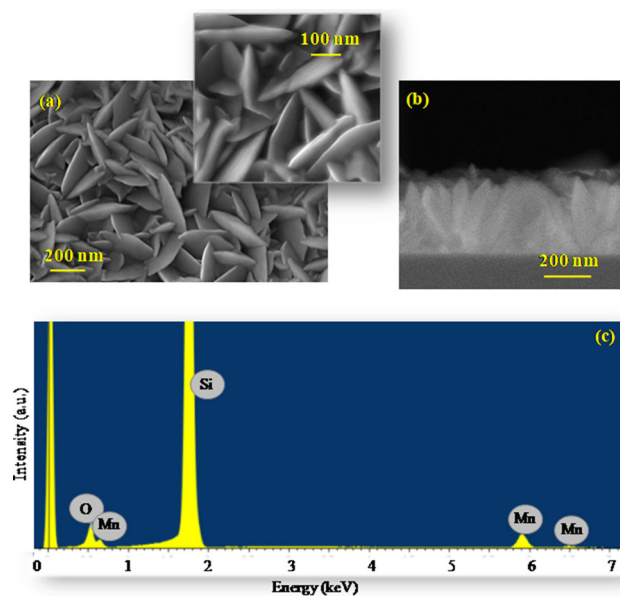


Figure 8. a) Plane-view and b) cross-sectional FE-SEM images of a Mn_3O_4 specimen deposited on Si(100) at 400°C from $\text{Mn}(\text{hfa})_2\text{-TMEDA}$. c) Corresponding energy dispersive X-ray spectroscopy (EDXS) results.

6.50 keV, as well as the $\text{O}_{\text{K}\alpha}$ signal at 0.52 keV. No evidence of C or F presence could be obtained, in agreement with the clean precursor decomposition discussed above. Irrespective of the analyzed region, in-plane EDXS analyses highlighted a homogeneous oxygen and manganese lateral distribution.

Efforts were also devoted to the characterization of systems supported on silica. In this regard, the surface morphology was investigated by atomic force microscopy (AFM, Figure 9a and b), which showed the presence of well interconnected protruding nanograins. The deposit appeared homogeneous and free

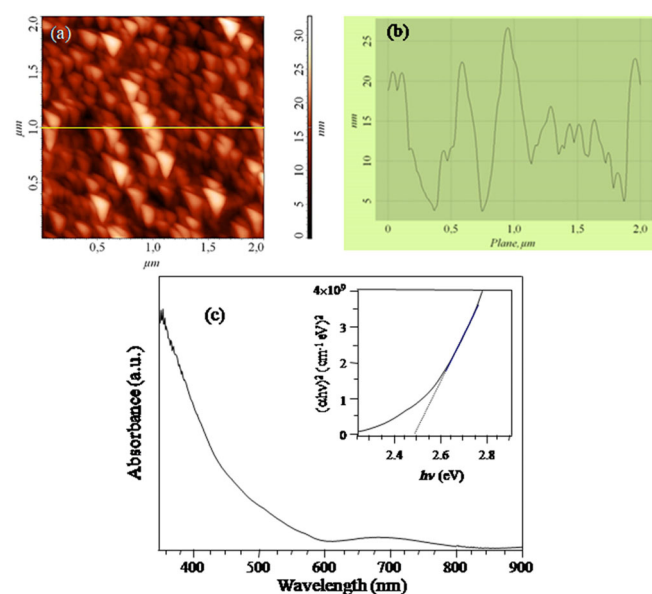


Figure 9. a) Representative AFM image; b) height profile along the marked line, and c) optical spectrum and derived Tauc plot for a Mn_3O_4 deposit obtained on SiO_2 at 400°C from $\text{Mn}(\text{hfa})_2\text{-TMEDA}$.

from cracks/pinholes. From the line height profile, a root-mean-square (RMS) roughness of 5 nm could be evaluated.

Finally, optical absorption analyses were carried out (Figure 9c). The spectral shape was in agreement with that reported for Mn_3O_4 -based materials.^[4] As observed, the system was almost transparent in the IR range, whereas significant absorption at lower wavelengths ($\lambda < 600$ nm) corresponded to inter-band transitions. The optical band gap was evaluated by the Tauc method, by plotting $(\alpha h\nu)^n$ versus $h\nu$ (Figure 9c, inset), with $n=2$ corresponding to direct allowed transitions,^[1d,33] and extrapolating the obtained trend to zero absorption. The estimated value ($E_G = 2.5$ eV) was in agreement with that previously reported for Mn_3O_4 ,^[4,5] and highlighted the efficient harvesting of visible light, paving the way to the use of the developed materials in solar-assisted applications.

Conclusion

This study was devoted to the preparation and combined experimental/theoretical characterization of two different Mn^{II} diamine diketonate adducts, of interest as molecular precursors for the vapor deposition of Mn oxide nanomaterials. The target molecular systems, $\text{Mn}(\text{hfa})_2\text{-TMEDA}$ and $\text{Mn}(\text{tfa})_2\text{-TMEDA}$, designed as alternatives to well-known manganese β -diketonates, differed by the presence of one $-\text{CF}_3$ group in the ligand chain. The two compounds, developed by a simpler route than that previously reported for $\text{Mn}(\text{hfa})_2\text{-TMEDA}$, are monomeric and water-free, thanks to the complete saturation of the Mn^{II} coordination environment. In particular, the presence of fluorine in the diketonate moieties played a key role in the stabilization of the complexes and in the obtainment of physico-chemical properties (thermal behavior and gas-phase reactivity) favorable for CVD/ALD applications.

The present results highlight that variations in the fluorine content of β -diketonate ligands do not affect appreciably the stability of these precursors to air and moisture. Differences in the behavior of the two compounds, as highlighted by ESI-MS fragmentation patterns, could mainly be related to different charge distributions in their molecular structures, depending on the nature of the β -diketonate ligand. Both precursors exhibit a higher volatility than that of conventional Mn β -diketonates, paving the way to their successful application in the vapor phase deposition of Mn oxides. Preliminary CVD experiments enabled the preparation of high purity, single-phase Mn_3O_4 nanomaterials endowed with tailored morphology, as well as an appreciable visible light absorption. These results suggest that the developed nanosystems are suitable candidates for possible technological end-uses in solar driven processes, ranging from photoactivated H_2O splitting to wastewater purification, as well as in the development of solid state gas sensing devices for the detection of toxic/flammable analytes (such as CO and CH_4). Additional attractive perspectives for this work will involve the extensive use of both molecular compounds in CVD/ALD processes, to explore in detail the interplay between processing parameters and the resulting material properties. Preliminary studies in these research areas are currently being carried out within our group.

Experimental Section

General

MnCl₂·4H₂O (98 + %), Hhfa (98 %), and Htfa (98 %) were purchased from Strem Chemicals® and TMEDA (≥ 98 %) from Merck®; all were used without further purification. All manipulations were carried out under normal laboratory conditions. Melting points (m.p.) were measured in air on a FALC melting point device at atmospheric pressure. Elemental analyses were carried out by using a Fisons Carlo Erba EA1108 apparatus (CHNS version).

Synthesis of Mn(hfa)₂·TMEDA

The synthesis of the target adduct was performed following a different procedure from that previously reported.^[11,17] Hhfa (3.4 mL, 23.30 mmol; *d* = 1.47 g mL⁻¹) was slowly added to a stirred aqueous solution of MnCl₂·4H₂O [2.37 g, 11.73 mmol, in deionized H₂O (50 mL)]. The subsequent dropwise addition of NaOH [0.93 g, 23.50 mmol, in deionized H₂O (10 mL)] yielded a clear yellow solution. TMEDA (1.9 mL, 12.59 mmol; *d* = 0.78 g mL⁻¹) was then slowly added to the reaction mixture, which turned to a maroon-like color. After reacting for 150 min in the dark, the obtained product was repeatedly extracted in dichloromethane until a completely colorless aqueous phase was obtained. The organic solution was thoroughly washed with deionized water and the solvent was removed at room temperature under reduced pressure (≈ 10⁻³ mbar), ultimately affording a yellow–orange solid (yield: 5.15 g, 75 %). M.p. 86 °C at 1 atm; elemental analysis calcd. (%) for C₁₆H₁₈O₄N₂F₁₂Mn (*M_w* = 585.25): C 32.84, H 3.10, N 4.79; found: C 33.60, H 2.90, N 4.78.

Synthesis of Mn(tfa)₂·TMEDA

Htfa (2.9 mL, 23.30 mmol; *d* = 1.27 g mL⁻¹) was slowly added to an aqueous solution of MnCl₂·4H₂O [2.37 g, 11.73 mmol, in deionized H₂O (50 mL)], maintained under vigorous stirring, resulting in phase separation. Subsequently, a solution of NaOH [0.93 g, 23.50 mmol, in deionized H₂O (10 mL)] was added dropwise, resulting in the formation of a yellow solution. TMEDA (1.9 mL, 12.59 mmol; *d* = 0.78 g mL⁻¹) was then added to the above mixture, which became maroon-like. After reaction in the dark for 150 min, the obtained product was repeatedly extracted in dichloromethane until the aqueous phase turned colorless. The organic solution was washed with deionized water and the solvent was removed at room temperature (≈ 10⁻³ mbar), yielding a light yellow solid (yield: 3.7 g, 66 %). M.p. 99 °C at 1 atm; elemental analysis calcd. (%) for C₁₆H₂₄O₄N₂F₆Mn (*M_w* = 477.31): C 40.26, H 5.07, N 5.87; found: C 40.93, H 5.10, N 6.03.

Both Mn(hfa)₂·TMEDA and Mn(tfa)₂·TMEDA were stored at room temperature and could be easily handled in air without any detrimental degradation. The powders were soluble in various solvents, such as hexane, dichloromethane, acetone, and alcohols. In both cases, crystals for X-ray analysis were obtained by re-dissolution in 1,2-dichloroethane, followed by slow solvent evaporation.

X-ray crystallography

Though the structure of Mn(hfa)₂·TMEDA has been previously reported,^[17] in this work crystallographic data were collected on both MnL₂·TMEDA compounds. In fact, since in the present work the Mn(hfa)₂·TMEDA compound was prepared through a synthesis procedure different from that previously reported,^[17] the first aim was to verify the possible formation of different Mn(hfa)₂·TMEDA poly-

morphs as a function of the adopted preparation route, as observed in the case of Cu(hfa)₂·TMEDA.^[13a] In addition, a key goal of this work was a detailed investigation of similarities and differences in the properties and behavior of MnL₂·TMEDA as a function of the ligand fluorination degree. Since the structure of Mn(tfa)₂·TMEDA has not been reported so far, an investigation of the molecular structures of both compounds under the same experimental conditions and with a similar refinement quality was performed to attain a direct comparison of experimental data pertaining to the two molecular systems. Furthermore, the simulation of compound properties, involving the electronic excitation analysis, the geometries of ions arising from their fragmentation, as well as the determination of their spin states, requires as a first step the optimization of the compound geometry, which, in turn, is based on the availability of structural data with a similar quality to compare and validate the results obtained by computational experiments.

XRD data for the synthesized compounds were collected on an Agilent Technologies SuperNova diffractometer, with an Atlas CCD detector, by using Cu_{Kα} radiation (*λ* = 1.54184 Å) from multilayer X-ray optics. The crystals were coated with a perfluoropolyether, picked up with a glass fiber, and mounted in the nitrogen cold gas stream of the diffractometer. The obtained data were processed with CrysAlisPro.^[34] An absorption correction based on multiple-scanned reflections was carried out with ABSPACK in CrysAlisPro. The crystal structure was solved by direct methods by using SHELXS-97 and refined with SHELXL-2013.^[35] For Mn(hfa)₂·TMEDA, two of the CF₃ groups showed rotational disorder. Disordered parts were modeled with appropriate restraints and constraints on geometry and atomic displacement parameters (ADPs). Anisotropic ADPs were introduced for all non-hydrogen atoms. Hydrogen atoms were placed in geometrically calculated positions and refined with the appropriate riding model.

CCDC 1585867 (Mn(hfa)₂·TMEDA) and 1585868 (Mn(tfa)₂·TMEDA) contain the supplementary crystallographic data for this paper. These data are provided free of charge by The Cambridge Crystallographic Data Centre

Analysis techniques

Optical spectroscopy analyses were carried out by using a Cary 50 spectrophotometer (Varian; spectral bandwidth = 1 nm). Measurements were carried out on 10⁻⁶ M solutions of Mn(hfa)₂·TMEDA and Mn(tfa)₂·TMEDA in ethanol, using quartz cuvettes (optical path = 0.5 cm).

ESI-MS characterization was carried out using a LCQ Fleet ion trap instrument (ThermoFisher), operating in both positive- and negative-ion modes. The used entrance capillary temperature and voltage were set at 250 °C and 4 kV, respectively. The 10⁻⁶ M solutions of the target Mn compounds in methanol were introduced by direct infusion with a syringe pump (flow rate = 8 μL min⁻¹). MSⁿ experiments were performed by applying a supplementary radio frequency (RF) voltage to the ion-trap end caps (5 V peak-to-peak).

TGA was performed with a TGA 2950 thermobalance manufactured by TA Instruments. Measurements were conducted under a pre-purified nitrogen atmosphere (heating rate = 10 °C min⁻¹) on samples that had a mass between 5 and 10 mg. DSC analyses were carried out by using a MDSC2920 apparatus (TA Instruments) equipped with a liquid nitrogen cooling system, using a heating rate of 3 °C min⁻¹.

Simulation

DFT calculations on Mn(hfa)₂-TMEDA and Mn(tfa)₂-TMEDA were performed with the PBE functional^[36] augmented with the long-range corrections of Hirao et al.^[37] The Gaussian 09 program was adopted,^[38] with Stuttgart–Dresden ECP pseudopotential for Mn and Stuttgart–Dresden basis set for all atoms.^[39] This basis set was enhanced with diffuse and polarization functions from the (D95++(d,p)) basis set,^[40] which provided a satisfactory description of other members of the M(hfa)₂-TMEDA series.^[13a,14a,15a,b,16] All calculated minima had positive frequencies and were in the high-spin state (sextet). The spin state was established by optimizing the geometry of the compounds in the sextet, quartet, and doublet states. Electronic excitations were calculated on the minimum-energy structures by time-dependent (TD) DFT. The 50 excitations at lower energy were considered. The spectra reported in Figure 2b were obtained by smoothing the TD-DFT excitations with a 2 nm Gaussian broadening. TD-DFT excitations were calculated for the two complexes also in ethanol, using a polarizable continuum model for the solvent.^[31] Natural bond orbital (NBO) wave function analyses were performed with NBO 5.0.^[41] The compound decomposition energies (ΔE) with respect to the fragments take into account the zero-point-energy contributions, and basis-set superposition errors were counterpoise-corrected. In addition to those in vacuum, ΔE values were also calculated in methanol with a polarizable continuum model.^[31]

CVD synthesis and characterization of Mn₃O₄ nanomaterials

Manganese oxide depositions were performed by means of a custom-built cold-wall CVD reactor,^[15a] using Mn(hfa)₂-TMEDA or Mn(tfa)₂-TMEDA precursors contained in an external glass reservoir. In this study, the precursor vaporization temperatures were kept at 60 and 65 °C for Mn(hfa)₂-TMEDA and Mn(tfa)₂-TMEDA, respectively, while the substrate temperature was 400 °C. Gas lines and valves connecting the precursor vessel and the reactor were maintained at $T \geq 100$ °C for each growth process to prevent precursor condensation. Depositions were carried out in O₂-based atmosphere for 1 h on 1 × 1 cm² Si(100) (MEMC[®], Merano, Italy) and HeraSil silica (Heraeus[®]) substrates, which were subjected to suitable pre-cleaning procedures before CVD experiments. For silicon substrates, the native SiO_x layer was removed prior to deposition by means of HF etching. O₂ [total flow rate = 200 standard cubic centimeters per minute (sccm)] was used as the carrier and reaction gas. Mass flow rates were controlled by MKS flow meters (Andover, USA). The total pressure, measured using a capacitance manometer (BOC Edwards, Crawley, UK), was set at 10.0 mbar.

XRD patterns were recorded in glancing-incidence mode ($\theta_i = 1^\circ$) on a Bruker D8 Advance X-ray diffractometer, equipped with a Cu_{K α} X-ray source (40 kV, 40 mA) and a Göbel mirror. Crystallite dimensions were estimated using the Scherrer equation.

FE-SEM analyses were performed by a Zeiss SUPRA 40 VP instrument, equipped with an Oxford INCA x-sight X-ray detector for EDXS investigation (primary beam voltage = 20 kV).

Optical absorption spectra for samples deposited on silica substrates were collected in transmission mode at normal incidence by means of a Cary 50 spectrophotometer, subtracting the substrate contribution. Tauc plots based on the obtained data were used to determine the optical band gap.

AFM measurements were performed using a NT-MDT SPM solver P47H-PRO apparatus, operating in tapping mode. RMS roughness values were obtained from the analysis of 2 × 2 μm^2 images after plane fitting.

Acknowledgements

We kindly acknowledge financial support under Padova University ex-60% 2014–2017, Insubria University FAR 2015–2016, P-DiSC #SENSATIONAL BIRD2016-UNIPD projects and ACTION post-doc fellowship. Thanks are also due to Dr. Loris Calore and Filippo Gri (Padova University), as well as Dr. Manuela Winter (Ruhr-University Bochum) for elemental microanalyses and useful experimental assistance.

Conflict of interest

The authors declare no conflict of interest.

Keywords: chemical vapor deposition • manganese oxides • Mn β -diketonates • nanomaterials • single-crystal X-ray diffraction

- [1] a) Z. Chen, Z. Jiao, D. Pan, Z. Li, M. Wu, C.-H. Shek, C. M. L. Wu, J. K. L. Lai, *Chem. Rev.* **2012**, *112*, 3833–3855; b) Z. Bai, B. Sun, N. Fan, Z. Ju, M. Li, L. Xu, Y. Qian, *Chem. Eur. J.* **2012**, *18*, 5319–5324; c) C. E. Frey, P. Kurz, *Chem. Eur. J.* **2015**, *21*, 14958–14968; d) L. Ben Said, A. Inoubli, B. Bouricha, M. Amlouk, *Spectrochim. Acta Part A* **2017**, *171*, 487–498; e) O. Nilsen, H. Fjellvåg, A. Kjekshus, *Thin Solid Films* **2003**, *444*, 44–51.
- [2] a) Z.-Y. Fei, B. Sun, L. Zhao, W.-J. Ji, C.-T. Au, *Chem. Eur. J.* **2013**, *19*, 6480–6487; b) K. Wang, X. Ma, Z. Zhang, M. Zheng, Z. Geng, Z. Wang, *Chem. Eur. J.* **2013**, *19*, 7084–7089; c) D. M. Robinson, Y. B. Go, M. Mui, G. Gardner, Z. J. Zhang, D. Mastrogianni, E. Garfunkel, J. Li, M. Greenblatt, G. C. Dismukes, *J. Am. Chem. Soc.* **2013**, *135*, 3494–3501.
- [3] M.-K. Song, S. Cheng, H. Chen, W. Qin, K.-W. Nam, S. Xu, X.-Q. Yang, A. Bongiorno, J. Lee, J. Bai, T. A. Tyson, J. Cho, M. Liu, *Nano Lett.* **2012**, *12*, 3483–3490.
- [4] D. P. Dubal, D. S. Dhawale, R. R. Salunkhe, V. J. Fulari, C. D. Lokhande, *J. Alloys Compd.* **2010**, *497*, 166–170.
- [5] a) D. P. Dubal, D. S. Dhawale, R. R. Salunkhe, S. M. Pawar, C. D. Lokhande, *Appl. Surf. Sci.* **2010**, *256*, 4411–4416; b) H. Y. Xu, S. L. Xu, X. D. Li, H. Wang, H. Yan, *Appl. Surf. Sci.* **2006**, *252*, 4091–4096.
- [6] L. Zhang, Q. Zhou, Z. Liu, X. Hou, Y. Li, Y. Lv, *Chem. Mater.* **2009**, *21*, 5066–5071.
- [7] H. W. Kim, Y. J. Kwon, H. G. Na, H. Y. Cho, C. Lee, J. H. Jung, *Microelectron. Eng.* **2015**, *139*, 60–69.
- [8] a) H. Van Bui, F. Grillo, J. R. van Ommen, *Chem. Commun.* **2017**, *53*, 45–71; b) S. M. George, *Chem. Rev.* **2010**, *110*, 111–131; c) H. Pedersen, S. D. Elliott, *Theor. Chem. Acc.* **2014**, *133*, 1476; d) J. S. Price, P. Chadha, D. J. H. Emslie, *Organometallics* **2016**, *35*, 168–180.
- [9] a) A. Devi, *Coord. Chem. Rev.* **2013**, *257*, 3332–3384; b) P. Marchand, C. J. Carmalt, *Coord. Chem. Rev.* **2013**, *257*, 3202–3221; c) L. McElwee-White, *Dalton Trans.* **2006**, 5327–5333; d) C. E. Knapp, C. J. Carmalt, *Chem. Soc. Rev.* **2016**, *45*, 1036–1064; e) S. Mishra, S. Daniele, *Chem. Rev.* **2015**, *115*, 8379–8448.
- [10] a) T. Nakamura, *Phys. Status Solidi C* **2015**, *12*, 958–963; b) T. Nakamura, R. Tai, T. Nishimura, K. Tachibana, *J. Electrochem. Soc.* **2005**, *152*, C584–C587; c) S. Dhar, A. Varade, S. A. Shivashankar, *Bull. Mater. Sci.* **2011**, *34*, 11–18; d) S. I. Troyanov, O. Y. Gorbenko, A. A. Bosak, *Polyhedron* **1999**, *18*, 3505–3509; e) S. Kang, G. Brewer, K. R. Sapkota, I. L. Pegg, J. Philip, *IEEE Trans. Nanotechnol.* **2012**, *11*, 437–440.
- [11] Z. Lipani, M. R. Catalano, P. Rossi, P. Paoli, G. Malandrino, *Chem. Vap. Deposition* **2013**, *19*, 22–28.
- [12] A. R. Merritt, R. Rajagopalan, J. D. Carter, *Thin Solid Films* **2014**, *556*, 28–34.
- [13] a) G. Bandoli, D. Barreca, A. Gasparotto, R. Seraglia, E. Tondello, A. Devi, R. A. Fischer, M. Winter, E. Fois, A. Gamba, G. Tabacchi, *Phys. Chem. Chem. Phys.* **2009**, *11*, 5998–6007; b) G. Bandoli, D. Barreca, A. Gasparotto, C. Maccato, R. Seraglia, E. Tondello, A. Devi, R. A. Fischer, M. Winter, *Inorg. Chem.* **2009**, *48*, 82–89.

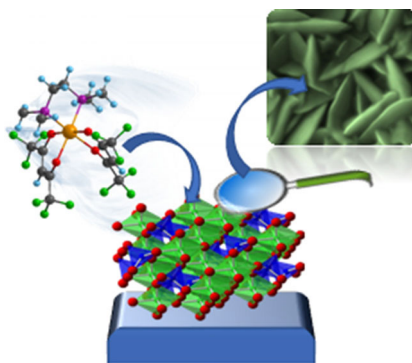
- [14] a) D. Barreca, E. Fois, A. Gasparotto, R. Seraglia, E. Tondello, G. Tabacchi, *Chem. Eur. J.* **2011**, *17*, 10864–10870; b) E. Fois, G. Tabacchi, D. Barreca, A. Gasparotto, E. Tondello, *Angew. Chem. Int. Ed.* **2010**, *49*, 1944–1948; *Angew. Chem.* **2010**, *122*, 1988–1992.
- [15] a) D. Barreca, G. Carraro, A. Devi, E. Fois, A. Gasparotto, R. Seraglia, C. Maccato, C. Sada, G. Tabacchi, E. Tondello, A. Venzo, M. Winter, *Dalton Trans.* **2012**, *41*, 149–155; b) D. Barreca, G. Carraro, A. Gasparotto, C. Maccato, R. Seraglia, G. Tabacchi, *Inorg. Chim. Acta* **2012**, *380*, 161–166; c) G. Tabacchi, E. Fois, D. Barreca, G. Carraro, A. Gasparotto, C. Maccato in *Advanced Processing and Manufacturing Technologies for Nanostructured and Multifunctional Materials II*, Wiley, Hoboken, **2015**, pp. 83–90.
- [16] G. Tabacchi, E. Fois, D. Barreca, A. Gasparotto, *Phys. Status Solidi A* **2014**, *211*, 251–259.
- [17] G. Malandrino, R. G. Toro, M. R. Catalano, M. E. Fragalà, P. Rossi, P. Paoli, *Eur. J. Inorg. Chem.* **2012**, 1021–1024.
- [18] F. A. Cotton, R. H. Holm, *J. Am. Chem. Soc.* **1960**, *82*, 2979–2983.
- [19] T. Yamada, T. Takai, O. Rhode, T. Mukaiyama, *Bull. Chem. Soc. Jpn.* **1991**, *64*, 2109–2117.
- [20] A. López-Periágo, O. Vallcorba, C. Frontera, C. Domingo, J. A. Ayllon, *Dalton Trans.* **2015**, *44*, 7548–7553.
- [21] N. A. Bailey, D. E. Fenton, M. V. Franklin, M. Hall, *J. Chem. Soc. Dalton Trans.* **1980**, 984–990.
- [22] W. B. S. McCormack, UK Patent GB 2022088A, **1979**.
- [23] G. Tabacchi, E. Fois, D. Barreca, A. Gasparotto, *Int. J. Quantum Chem.* **2014**, *114*, 1–7.
- [24] B. S. Lim, A. Rahtu, J.-S. Park, R. G. Gordon, *Inorg. Chem.* **2003**, *42*, 7951–7958.
- [25] L.-Y. Wang, X.-Q. Wang, K. Jiang, J.-L. Chang, Y.-F. Wang, *J. Mol. Struct.* **2007**, *840*, 14–21.
- [26] F. H. Allen, *Acta Crystallogr. Sect. B* **2002**, *58*, 380–388.
- [27] H. Wang, Z. Liu, C. Liu, D. Zhang, Z. Lü, H. Geng, Z. Shuai, D. Zhu, *Inorg. Chem.* **2004**, *43*, 4091–4098.
- [28] D. Luneau, C. Stroh, J. Cano, R. Ziessel, *Inorg. Chem.* **2005**, *44*, 633–637.
- [29] J. Ni, H. Yan, A. Wang, Y. Yang, C. L. Stern, A. W. Metz, S. Jin, L. Wang, T. J. Marks, J. R. Ireland, C. R. Kannewurf, *J. Am. Chem. Soc.* **2005**, *127*, 5613–5624.
- [30] L. Wang, Y. Yang, J. Ni, C. L. Stern, T. J. Marks, *Chem. Mater.* **2005**, *17*, 5697–5704.
- [31] M. Cossi, V. Barone, B. Mennucci, J. Tomasi, *Chem. Phys. Lett.* **1998**, *286*, 253–260.
- [32] Pattern No. 024-0734, JCPDS (2000).
- [33] B. D. Vriezicke, S. Patel, B. E. Davis, D. P. Birnie, *Phys. Status Solidi B* **2015**, *252*, 1700–1710.
- [34] CrysAlisPro Software System, version 1.171.36.20; Agilent Technologies UK Ltd.: Oxford, U. K., **2012**.
- [35] G. Sheldrick, *Acta Crystallogr. Sect. A* **2008**, *64*, 112–122.
- [36] J. P. Perdew, K. Burke, M. Ernzerhof, *Phys. Rev. Lett.* **1996**, *77*, 3865–3868.
- [37] a) H. Iikura, T. Tsuneda, T. Yanai, K. Hirao, *J. Chem. Phys.* **2001**, *115*, 3540–3544; b) A. W. Lange, M. A. Rohrdanz, J. M. Herbert, *J. Phys. Chem. B* **2008**, *112*, 6304–6308; c) J.-W. Song, T. Hirose, T. Tsuneda, K. Hirao, *J. Chem. Phys.* **2007**, *126*, 154105.
- [38] Gaussian 09, Revision D.02, M. J. Frisch, G. W. Trucks, H. B. Schlegel, G. E. Scuseria, M. A. Robb, J. R. Cheeseman, G. Scalmani, V. Barone, B. Mennucci, G. A. Petersson, H. Nakatsuji, M. Caricato, X. Li, H. P. Hratchian, A. F. Izmaylov, J. Bloino, G. Zheng, J. L. Sonnenberg, M. Hada, M. Ehara, K. Toyota, R. Fukuda, J. Hasegawa, M. Ishida, T. Nakajima, Y. Honda, O. Kitao, H. Nakai, T. Vreven, J. A. Montgomery, Jr., J. E. Peralta, F. Ogliaro, M. Bearpark, J. J. Heyd, E. Brothers, K. N. Kudin, V. N. Staroverov, R. Kobayashi, J. Normand, K. Raghavachari, A. Rendell, J. C. Burant, S. S. Iyengar, J. Tomasi, M. Cossi, N. Rega, J. M. Millam, M. Klene, J. E. Knox, J. B. Cross, V. Bakken, C. Adamo, J. Jaramillo, R. Gomperts, R. E. Stratmann, O. Yazyev, A. J. Austin, R. Cammi, C. Pomelli, J. W. Ochterski, R. L. Martin, K. Morokuma, V. G. Zakrzewski, G. A. Voth, P. Salvador, J. J. Dannenberg, S. Dapprich, A. D. Daniels, Ö. Farkas, J. B. Foresman, J. V. Ortiz, J. Cioslowski, D. J. Fox, Gaussian, Inc., Wallingford, CT, **2009**.
- [39] A. Bergner, M. Dolg, W. Küchle, H. Stoll, H. Preuß, *Mol. Phys.* **1993**, *80*, 1431–1441.
- [40] T. H. Dunning, Jr., P. J. Hay in *Modern Theoretical Chemistry*, Vol. 2, Chap. 1, Plenum, New York, **1976**.
- [41] a) L. Goodman, R. R. Sauer, *J. Comput. Chem.* **2007**, *28*, 269–275; b) A. E. Reed, L. A. Curtiss, F. Weinhold, *Chem. Rev.* **1988**, *88*, 899–926; c) E. D. Glendening, J. K. Badenhoop, A. E. Reed, J. E. Carpenter, J. A. Bohmann, C. M. Morales, F. Weinhold in *NBO 5.0, Theoretical Chemistry Institute, University of Wisconsin, Madison, USA*, **2001**.

Manuscript received: July 24, 2017

Version of record online: ■■■■■ 0000

FULL PAPER

Producing perfect precursors: A convenient route for the synthesis of Mn^{II} diamine diketonate complexes is proposed. For the first time, the target adducts are characterized in detail by a combined experimental-theoretical approach. The compounds possess a monomeric structure, very favorable mass-transport properties, and a clean fragmentation, all of which make them promising precursors for the vapor phase fabrication of manganese oxide nanosystems (see figure).



Chemical Vapor Deposition

C. Maccato, L. Bigiani, G. Carraro, A. Gasparotto, R. Seraglia, J. Kim, A. Devi, G. Tabacchi, E. Fois, G. Pace, V. Di Noto, D. Barreca**

■■ - ■■

Molecular Engineering of Mn^{II} Diamine Diketonate Precursors for the Vapor Deposition of Manganese Oxide Nanostructures 